Neutron diffraction, muon-spin rotation, and high magnetic field investigation of the multiferroic antiferromagnetic quantum spin-chain system $CuCrO_4$

J. M. Law,[1,2] H. Luetkens,[3] G. Pascua,[3,4] Th. Hansen,[5] R. Glaum,[6] Z.-S. Wang,[1] J. Wosnitza,[1] and R. K. Kremer[2]

[1]*Hochfeld-Magnetlabor Dresden (HLD-EMFL) and Würzburg-Dresden Cluster of Excellence ct.qmat, Helmholtz-Zentrum Dresden-Rossendorf, 01328 Dresden, Germany*

[2]*Max-Planck-Institut für Festkörperforschung, D-70569 Stuttgart, Germany*

[3]*Laboratory for Muon-Spin Spectroscopy, Paul Scherrer Institut, CH-5232 Villigen PSI, Switzerland*

[4]*Hochschule Luzern, IMT-Biotechnology Space Support Center (ESA-USOC), 6052 Hergiswil, Switzerland*

[5]*Institut Laue-Langevin, 38042 Grenoble, France*

[6]*Institut für Anorganische Chemie, Universität Bonn, Gerhard-Domagk-Strasse 1, 53121 Bonn, Germany*

(Received 8 November 2022; revised 17 April 2023; accepted 22 May 2023; published 30 May 2023)

Multiferroic behavior in the linear-chain spin $S = 1/2$ compound $CuCrO_4$ was proposed to appear due to competing nearest- and next-nearest-neighbor exchange interactions along the chain. Here, we report on our study of the long-range magnetic ordering using powder neutron diffraction and muon-spin rotation measurements. Consistently, both methods find incommensurate long-range antiferromagnetic ordering below 8.5(3) K. We determined the magnetic structure from neutron powder diffraction patterns based on the propagation vector $\vec{\tau} = (0, 0, 0.546(1))$. At 1.9 K, the magnetic moment of Cu^{2+} was refined to 0.48(2) μ_B. The Cu moments form a helicoidal spiral with an easy plane coinciding with the equatorial planes of the Jahn-Teller elongated CuO_6 octahedra. Low-temperature high magnetic field measurements of the magnetization and the dielectric polarization show the multiferroic phase to extend up to ∼25 T, after which a new, yet unknown phase appears. Full saturation of the magnetic moment is expected to occur at fields much beyond 60 T.

DOI: 10.1103/PhysRevB.107.184442

I. INTRODUCTION

Systems with multiple ferroic order parameters are widely investigated to understand their coupling mechanisms but also to explore potential technological applications [1]. For example, controlling ferroelectric polarization by a magnetic field or switching magnetization by an electric field are considered to enable substantial progress in modern energy-efficient digital data storage devices [2,3]. The quest to understand the underlying physical principles of the coupling mechanisms will benefit from the identification and characterization of new multiferroic systems.

To this end, we have studied a number of antiferromagnetic (AFM) $S = 1/2$ low-dimensional magnets with competing nearest-neighbor (NN) and next-nearest-neighbor (NNN) intrachain spin-exchange interactions. About a decade ago, the phase diagram of such NN-NNN frustrated spin $S = 1/2$ quantum spin chains was intensively investigated theoretically by Läuchli *et al.* [4], Furukawa *et al.* [5], and Sato *et al.* [6]. For ferromagnetic (FM) NN and AFM NNN exchange ($J_{NN}/J_{NNN} < 0$) and a small easy-plane anisotropy the phase diagram exhibits an extended sector with chiral magnetic order which enables type-II multiferroic behavior. Prominent examples of the NN-NNN scenario, among others (see, e.g., Ref. [7]), are $LiCuVO_4$ or the binary cupric halides CuX_2 (X = Cl, Br) [8–12]. Lately, $LiCuVO_4$ has gained special attention because in strong magnetic fields it realizes bond and spin-nematic phases [13,14].

Competition of NN and NNN exchange interaction in linear-chain systems is prominently found in systems that contain so-called "ribbon chains" where the magnetic entities center anion square plaquettes that connect via opposite edges to infinite chains. NNN exchange through super-superexchange via two intermediates, e.g., O^{2-} anions, generally being antiferromagnetic, usually dominates in magnitude, whereas the NN exchange is often found to be weakly ferromagnetic, with, however, its sign and magnitude depending critically on the bonding angles and distances to the connecting anions [15,16]. A system which shows opposite behavior, i.e., where the NN interaction is FM and larger in magnitude than the NNN AFM exchange, is the mineral trippkeite with composition $CuAs_2O_4$, which exhibits FM long-range magnetic ordering (LRO) below ∼7 K [17,18].

In the course of our investigation of spin $S = 1/2$ frustrated linear-ribbon-chain systems, we identified $CuCrO_4$ as a new type-II multiferroic system. $CuCrO_4$ with Cu in the oxidation state +2, i.e., a hole in the 3*d* shell, and Cr in the unusual oxidation state of +6, i.e., with an empty 3*d* shell, crystallizes in the $CrVO_4$ structure type (see Fig. 1) [19]. The structural and magnetic properties of materials crystallizing with the $CrVO_4$ structure type, including 3*d*

Published by the American Physical Society under the terms of the Creative Commons Attribution 4.0 International license. Further distribution of this work must maintain attribution to the author(s) and the published article's title, journal citation, and DOI. Open access publication funded by the Max Planck Society.

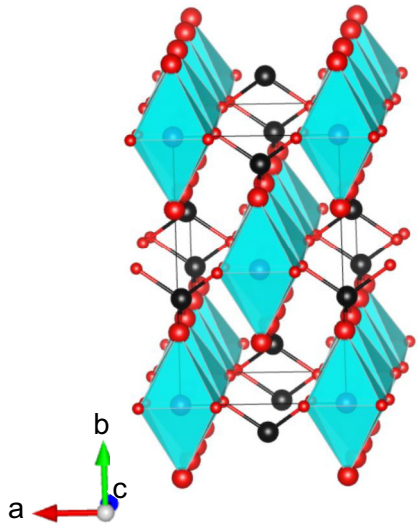

FIG. 1. Crystal structure of $CuCrO_4$ at 2 K as derived from the profile refinement of the HRPT 2-K NPD pattern. The blue and black spheres represent Cu and Cr cations, respectively. The oxygen atoms O1 (apical) and O2 (equatorial) are shown as red spheres. The diameters of the spheres correspond to the isotropic displacement parameters listed in Table I.

transition metal phosphates, anhydrous sulfates, selenates, or vanadates, have been extensively investigated over the past six decades [20]. Early investigated examples are $CrVO_4$ (Ref. [21]), $MnSO_4$ (Refs. [22,23]), β-$CrPO_4$ (Refs. [24,25]), VPO_4 (Refs. [26,27]), and $TiPO_4$ (Refs. [26,27]). Generally, these systems exhibit low-dimensional magnetic behavior [26,28] and tend to order with cycloidal or helical magnetic structures. For β-$CrPO_4$ Luo and Wang have recently observed multiferroicity below 23 K [29]. Lately, $TiPO_4$ has attracted particular attention [27,30–34]. $TiPO_4$ features very strongly NN exchange coupled ($\sim$80 meV) $S = 1/2$ Ti^{3+} linear chains, which below 74 K spin-Peierls dimerize to a nonmagnetic ground state accompanied by a structural phase transition. Preceding this phase transition is a structurally and magnetically incommensurate regime extending up to 111 K.

In a first characterization of the magnetic and dielectric properties of $CuCrO_4$, Law *et al.* found that $CuCrO_4$ represents a quasi-one-dimensional Heisenberg system with competing NN and NNN interactions, both being AFM, unlike most of the analogous frustrated ribbon-chain systems studied before [31]. The ratio of the exchange interactions amounts to $J_{NN}/J_{NNN} \approx 2$, which places $CuCrO_4$ in the vicinity of the Majumdar-Ghosh point [35,36]. In the same work [31], $CuCrO_4$ was shown to order antiferromagnetically and to be multiferroic as evidenced, e.g., by a large magnetodielectric anomaly at the Néel temperature of $\sim$8.5 K.

Here, we extend these investigations by probing the low-temperature crystal structure and, in particular, the LRO phase in zero field by neutron powder diffraction (NPD), muon-spin rotation, and field-dependent magnetization and dielectric polarization measurements. Our neutron diffraction and muon-spin rotation (μSR) studies identify the magnetic structure as an incommensurate helicoidal phase. Measurements of the magnetization up to magnetic fields of $\sim$60 T provide insight as to under which magnetic fields the incommensurate ground state and the multiferroicity remain stable.

II. EXPERIMENT

A large powder sample of $CuCrO_4$ was precipitated from an aqueous solution as described in detail previously [19,27,31]. To reduce incoherent neutron scattering from protons adherent to the surface of the powder grains, the sample employed for neutron scattering was synthesized using exclusively D_2O (99.8% enrichment) rather than natural water. Initially, phase purity of the samples was checked by x-ray powder diffraction with a D8 Advance powder diffractometer (Bruker, Berlin, Germany) using Mo $K_{\alpha 1}$ radiation. High-resolution neutron powder diffraction patterns at 2 and 20 K were collected on a $\sim$8.5 g sample using the High-Resolution Powder Diffractometer for Thermal Neutrons (HRPT) at the Paul Scherrer Institute (Villigen, Switzerland) [37]. Medium-resolution NPD patterns between 1.9 and 20 K were measured using neutrons with a wavelength of 2.426 Å on the high-intensity, variable-resolution powder diffractometer D20 at the Institute Laue-Langevin (ILL; Grenoble, France) [38]. Rietveld profile refinements of the diffraction patterns were performed with the FULLPROF software package [39]. In the case of the HRPT data, an instrumental resolution file was used. High field magnetization and dielectric capacitance measurements were collected at the Dresden High Magnetic Field Laboratory (HLD-EMFL) employing a compensated-coil technique (sample size $\sim$ 50 mg) and a balanced capacitance bridge (GR1615-A; General Electric) [40,41]. Low field ($\leqslant$7 T) magnetization data were collected with a Magnetic Properties Measurement System (7 T MPMS; Quantum Design). Dielectric capacitance data up to $\leqslant$ 12 T were measured in a ^{4}He cryostat employing an AH 2700A capacitance bridge (Andeen-Hagerling). The high field magnetization measurements were adjusted to match low field data taken on the identical sample with a superconducting quantum interference device (SQUID) magnetometer. Muon-spin rotation spectra were measured on the General Purpose Surface (GPS) muon spectrometer at the Paul Scherrer Institute in the temperature range from 160 to 2.5 K.

III. RESULTS AND DISCUSSION

A. Low-temperature crystal structure

$CuCrO_4$ crystallizes with the $CrVO_4$ structure type characterized by corrugated ribbons of trans-edge connected Jahn-Teller elongated CuO_6 octahedra [19]. These are connected to neighboring ribbon chains by distorted CrO_4 tetrahedra, which link two equatorial oxygen atoms from neighboring chains in the $a-c$ plane and two apical oxygen atoms from octahedral strands above or below (see Fig. 1). Already noticeable from the single-crystal x-ray data reported by Seferiadis and Oswald [19] are the markedly different displacement parameters for the atoms indicating an oblate displacement ellipsoid in the $b-c$ plane for the Cr atoms but rather spherical ellipsoids for the apical oxygen atoms (labeled as O1 in Table I). Remarkably, the latter are markedly

TABLE I. Lattice parameters, fractional coordinates, isotropic displacement parameters, and conventional reliability indicators of $CuCrO_4$ as obtained from the Rietveld profile refinement (FULLPROF) of the NPD patterns measured using neutrons with a wavelength of $\lambda = 1.8857$ Å at $T = 20$ and 2 K, respectively. The Rietveld profile refinements were performed assuming the space group *Cmcm* (No. 63). Site occupancies within error bars converged to their stoichiometric values and were fixed in the final refinements. The refined patterns at 20 and 2 K are displayed in Fig. 2.

	20 K	2 K
a (Å)	5.45189(9)	5.45193(9)
b (Å)	8.9594(2)	8.9600(2)
c (Å)	5.8665(1)	5.8658(1)
V (Å)^3	286.55(1)	286.54(1)
Cu 4*a*		
x	0	0
y	0	0
z	0	0
B_{iso} (Å^2)	0.34(5)	0.33(5)
Cr 4*c*		
x	0	0
y	0.3658(6)	0.3665(5)
z	$\frac{1}{4}$	$\frac{1}{4}$
B_{iso} (Å^2)	0.80(9)	0.76(8)
O1 8*f*		
x	0	0
y	0.2664(2)	0.2664(2)
z	0.0289(3)	0.0289(3)
B_{iso} (Å^2)	0.88(5)	0.88(5)
O2 8*g*		
x	0.2341(3)	0.2343(3)
y	−0.0188(2)	−0.0189(2)
z	$\frac{1}{4}$	$\frac{1}{4}$
B_{iso} (Å^2)	0.40(5)	0.38(5)
Bragg R factor (%)	3.54	3.46
Bragg R_f factor (%)	2.39	2.33

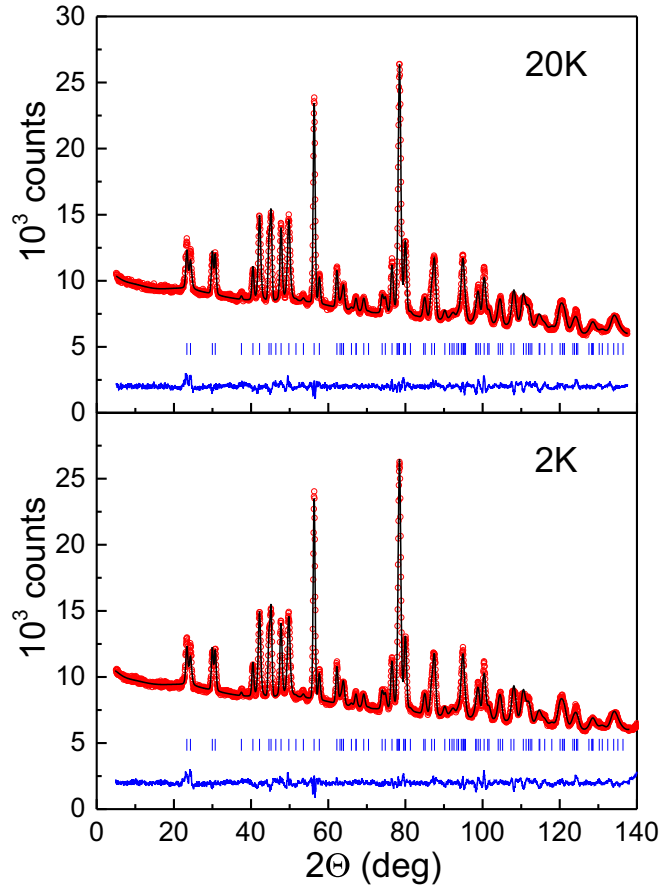

FIG. 2. NPD patterns of $CuCrO_4$ collected at the multidetector neutron diffractometer HRPT at 20 K (top) and 2 K (bottom) using neutrons of 1.8857 Å wavelength. Magnetic Bragg reflections are not resolved in the 2-K pattern. The red circles represent the measured data, and the black solid line is the result of the Rietveld profile refinement. The blue solid line at the bottom of the graph shows the difference between the observed and calculated patterns. The vertical blue ticks mark the angles of the Bragg reflections used to calculate the refined pattern.

enlarged as compared with the displacement of the oxygen atoms in the equatorial plane (labeled as O2 in Table I) [19].

This observation points to an increased dynamics of the CrO_4 tetrahedra and the apical oxygen atoms which may induce a vibrationally induced modulation of the corrugated CuO_6 strands and possibly enhanced magnetoelastic coupling. In order to investigate whether such atom motion may also lead to a significant structural modification or even a structural phase transition at low temperatures, we have collected high-resolution neutron powder diffraction patterns at 20 K and at 2 K (Fig. 2) and determined the structural parameters from profile refinements. The structural parameters obtained from Rietveld profile refinements of the diffraction patterns are compiled in Table I. All Bragg reflections of the low-temperature NPD patterns could be indexed based on the space group *Cmcm* indicating that the room temperature structure is preserved at low temperatures [19]. We did not observe additional Bragg reflections from impurity phases, proving the phase purity of our sample. Apart from some thermal contraction the lattice parameters and the atom positional parameters derived from the profile refinement are close to those found at room temperature (cf. Table I). An inspection of some characteristic Bragg reflections also gave no indication of noticeably different widths indicative of a structural distortion or internal strain.

B. High field magnetization and ferroelectricity

The magnetization isotherm at 2.7 K measured in pulsed magnetic fields on a compacted powder pellet of $CuCrO_4$ is shown in the inset of Fig. 3(a). At 60 T, a moment of $\sim$0.45 μ_B/f.u. was found. The expected saturation value, $g \cdot S = 1.07\ \mu_B/Cu^{2+}$, can be extrapolated to occur beyond > 100 T. Shown in Fig. 3(a) is the magnetic susceptibility of $CuCrO_4$ up to 30 T. The low-temperature, 2.7-K, data can be accounted for by invoking a paramagnetic impurity yielding a Curie-like tail, in addition to the signal from the antiferromagnetic bulk sample. Accordingly, the magnetization was approximated by the function

$$\chi(H,T) \propto A\frac{d\mathcal{B}_J(H,T)}{dH(T)} + B + C \times H, \qquad (1)$$

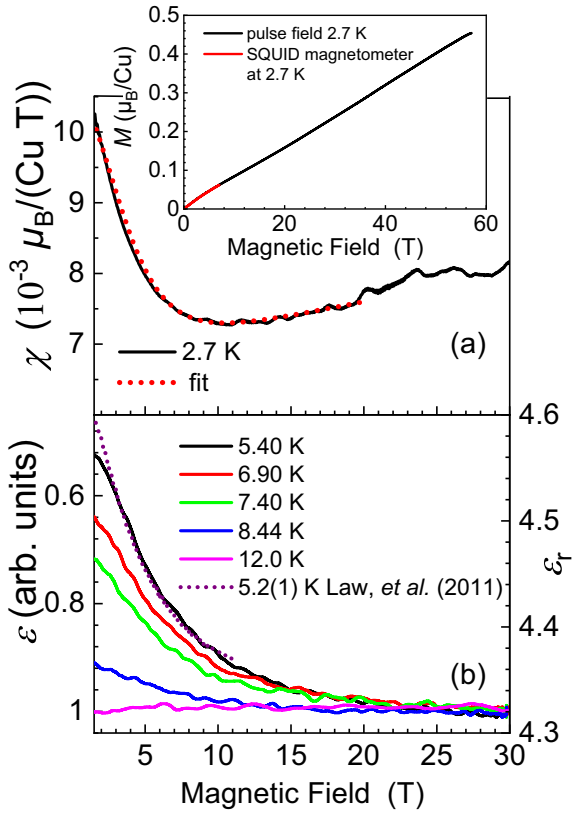

FIG. 3. (a) Solid black line: The measured magnetic susceptibility, at 2.7 K, vs external magnetic field. The dotted red line is a fit to the data; see text for details. Inset: Magnetization vs applied magnetic field; the solid black line represent the pulsed-field collected data, and the solid red line is for the same sample measured in a SQUID magnetometer. (b) The real part of the dielectric permittivity measured in pulsed field (solid lines, left axis), and relative dielectric permittivity measured in dc fields, from Ref. [31] (dotted line, right axis).

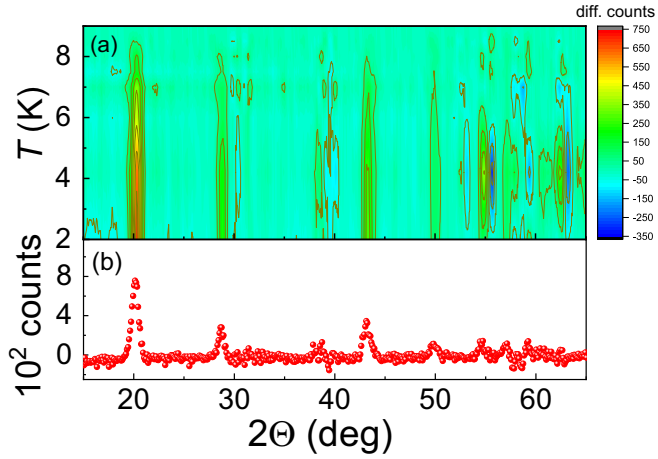

FIG. 4. (a) Heat map of the difference between neutron powder diffraction patterns of $CuCrO_4$ measured between 1.9 and 9 K. The powder diffraction pattern taken at 9 K was subtracted to suppress nuclear scattering. The patterns have been collected with neutrons of a wavelength of 2.426 Å on ILL's medium-resolution high-intensity powder diffractometer, D20. Here, diff. counts, difference counts. (b) Difference of two neutron powder diffraction patterns collected at 1.9 and 9 K.

where $\mathcal{B}_J$ is the Brillouin function for $S = 1/2$, A is the fractional contribution of the impurity, and the parameters B and C model the behavior of the bulk sample.

As can be seen in Fig. 3, Eq. (1) fits the data very well assuming a 1.5 mol % $S = 1/2$ impurity with a g factor of 2. Similar paramagnetic impurity fractions have been seen previously in another sample of $CuCrO_4$ [31]. At higher fields (∼25 T) a smeared shoulderlike feature is visible, which we ascribe to a high field crossover from the AFM multiferroic phase to a presently unknown phase. The shoulder in the magnetization is paralleled by the suppression of the dielectric susceptibility increase (see below).

High field measurements of the dielectric permittivity [Fig. 3(b)] agree quantitatively with low field data reported by Law *et al.* [31]. Above the LRO temperature the dielectric permittivity is essentially field independent, whereas below the LRO the low-temperature increase of the zero-field dielectric permittivity is suppressed by the application of a magnetic field. At magnetic fields above ∼25 T the permittivity becomes field independent indicating that a multiferroic phase is no longer present.

C. Magnetic structure determination

Below ∼9 K, high-intensity medium-resolution neutron powder diffraction patterns collected on ILL's powder diffractometer, D20, between 20 and 1.9 K revealed additional Bragg reflections in the low-angle 2Θ regime. These can be clearly assigned to magnetic scattering by their temperature dependence. Difference patterns obtained by subtracting the 9-K pattern to suppress the strong nuclear scattering are displayed in a color-coded contour plot in Fig. 4. Clearly unveiled is the strongest magnetic Bragg reflection at 20.1° ($D = 6.95$ Å), the integrated intensity of which (cf. Fig. 5) falls off with a power law according to Eq. (2). A least-squares fit to the integrated intensities indicates a critical temperature T_c of 8.42(9) K, in very good agreement with our earlier findings [31].

$$I(T) \propto (1 - (T/T_c))^{-2\beta}. \tag{2}$$

Additional, though weaker magnetic Bragg reflections are also revealed at approximately 28.9°, 43.3°, 50.0°, and possibly 58.8°, all disappearing above ∼9 K. The magnetic Bragg reflections could be readily indexed based on the propagation vector

$$\vec{\tau} = (0, 0, \sim 0.55),$$

indicating an incommensurate magnetic structure along [001], i.e., along the Cu chains, similar to what has been found for analogous systems such as $LiCuVO_4$ or the copper dihalides CuX_2 (X = Cl, Br) [8,9,12].

A solution of the magnetic structure and refinement of the moment magnitude and direction was achieved based on the difference of the diffraction patterns collected at 1.9 and 9 K. The best model of the magnetic structure requires magnetic Cu atoms with the same magnitude for the magnetic moment at positions (0,0,0) and (0.5,0.5,0) in the nuclear cell and assumes them to be collinear but antiparallel. Along [001],

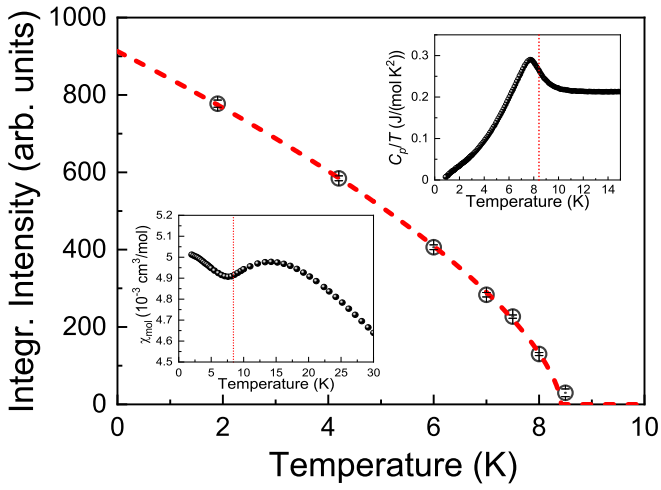

FIG. 5. Integrated intensity vs temperature of the 20.1° ($D = 6.95$ Å) magnetic Bragg reflection. The red dashed line represents a fit of a power law according to Eq. (2) to the data points indicating a Néel temperature of $T_c = 8.42(9)$ K and a critical exponent β of 0.32(2). Error bars are of the size of the symbols. The upper and the lower insets display the heat capacity and the magnetic susceptibility (7 T), respectively, taken from Ref. [31]. In the insets the dotted vertical bars mark the critical temperature T_c.

the Cu^{2+} moments form helices spiraling in the $a-c$ plane as the easy plane with a pitch angle of ∼100°. The result of the profile refinement of the difference pattern is displayed in Fig. 6. Determining the scale factor from a full profile

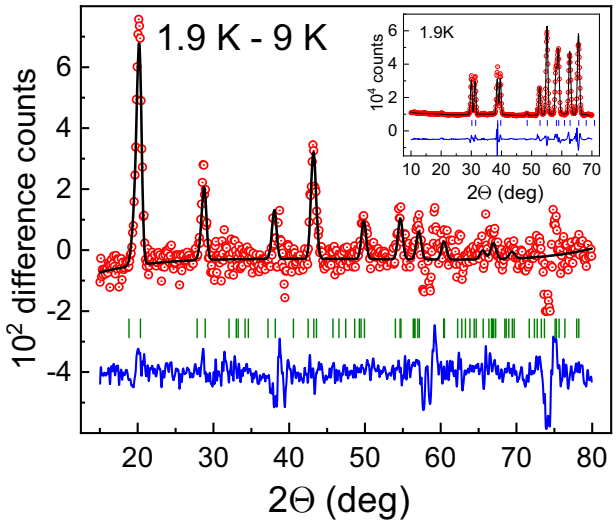

FIG. 6. Difference of the neutron powder diffraction patterns of $CuCrO_4$ collected at 1.9 and 9 K using neutrons with a wavelength of 2.426 Å. The inset displays the pattern at 1.9 K with a profile refinement assuming nuclear contributions only. Scaling factors are identical in both Rietveld refinements. The red circles represent the measured data, and the black solid lines are the result of the profile refinement. The blue solid line at the bottom of the graph shows the difference between the observed and calculated patterns. The vertical green ticks mark the angles of the magnetic Bragg reflections used to calculate the refined pattern.

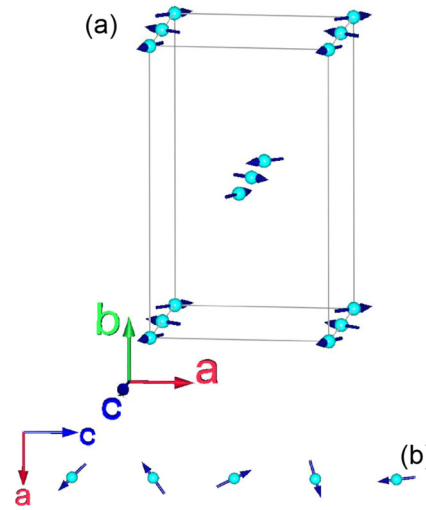

FIG. 7. (a) Magnetic structure of $CuCrO_4$ at 1.9 K. Two nuclear unit cells are outlined. The ordered moment per Cu atom amounts to 0.48(1) μ_B. (b) Projection along [010] of the helicoidal spiral propagating along the crystallographic c axis with $\vec{\tau}_c = 0.546(1)$.

refinement of the nuclear structure using the pattern collected at 1.9 K and fixing the scale factor in the refinement of the magnetic structure (see Fig. 7) results in a magnetic moment of

$$|\vec{\mu}| = 0.48(1)\ \mu_B,$$

close to what has been observed in similar incommensurate helicoidal systems such as $LiCuVO_4$, $CuCl_2$, and $CuBr_2$ [8,9,12].

D. μSR measurements

Zero-field μSR spectra have been taken at temperatures between 160 and 2.5 K. In Figs. 8 and 9, characteristic μSR

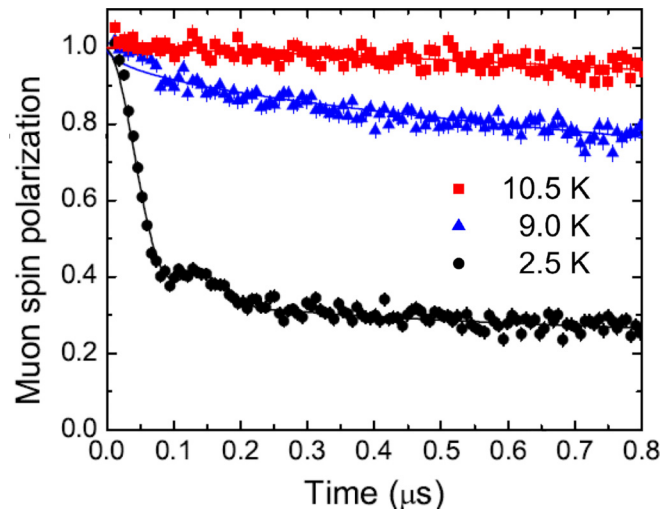

FIG. 8. Zero-field μSR spectra on a short time scale. Note the strongly damped oscillation at 2.5 K indicative of long-range magnetic order with a broad internal-field distribution at magnetically inequivalent muon deposition sites.

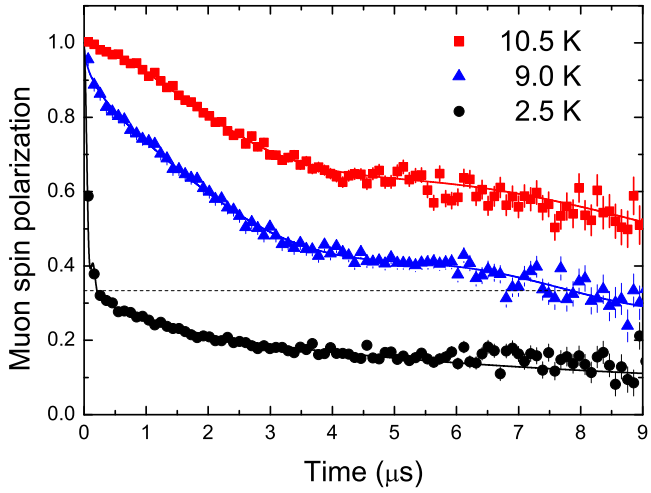

FIG. 9. Zero-field μSR spectra on a long time scale. Note the unusual functional form at high temperatures showing the presence of at least two crystallographically inequivalent muon sites. The spectrum at 2.5 K proves the presence of magnetic dynamics at this temperature since the long-time polarization falls below 1/3 (dashed line); see text.

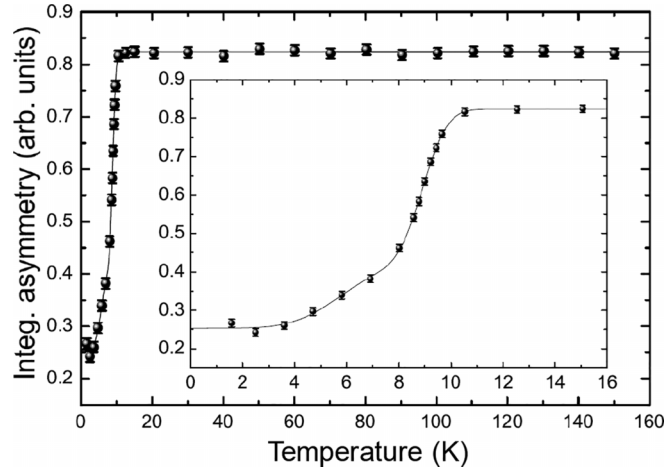

FIG. 10. Time-integrated muon-spin polarization, showing the onset of electronic relaxation below ~9 K and the absence of a magnetic anomalies between 10 and 160 K. The inset displays an enlarged view of the low-temperature region.

spectra are displayed for selected temperatures on a short and a long time scale, respectively. At high temperatures, the spectra exhibit a weak depolarization characteristic caused by the presence of a magnetic field distribution at the muon site due to static nuclear moments only. The functional form of the spectrum could be successfully modeled by a superposition of two subspectra indicating the presence of at least two crystallographically inequivalent muon deposition sites. Below ~9 K, relaxation due to magnetic moments sets in, which is characterized by a strong relaxation of 2/3 of the signal followed by a weak relaxation of the remaining 1/3 of the signal. This behavior is typical for powder samples, where in a spatial average 2/3 of the internal-magnetic-field components are perpendicular to the initial muon spin and give rise to a precession signal. The very strong damping of the μSR oscillation indicates that below ~9 K, LRO with a broad field distribution at the muon sites sets in. The width of the internal-field distribution suggests a magnetic structure comprising a distribution of magnetically inequivalent muon sites, consistent with an incommensurate magnetic structure. Particularly because of the presence of at least two different crystallographic muon deposition sites, a conclusive theoretical modeling of the spectra is hampered. Only within limited time intervals can the data be well described, and as a first approach we therefore performed a model-independent analysis using a weighted integration of the time-dependent polarization $P(t)$. Consequently, the integration masks more detailed microscopic information from a correct model, though not at hand at present. The quantity $I(T)$ calculated according to

$$I(T) = \frac{1}{\tau_\mu} \int_0^\infty e^{-t/\tau_\mu} P(t) dt, \tag{3}$$

with τ_μ being the muon lifetime, is displayed in Fig. 10. Any additional depolarization caused by electronic moments, either dynamic or static, will lead to a reduction of this quantity with respect to the high-temperature value, where depolarization is due to nuclear moments only. Figure 10 indicates that strong electronic relaxation sets in below ~9 K. Further magnetic anomalies between 10 and 160 K could not be discerned. In an attempt to analyze the time dependence and to follow the strongly damped oscillation versus temperature we tested various models and obtained an acceptable parametrization of the spectra. However, these models are partially difficult to justify physically. The damped oscillation is best described by a Gaussian damped Bessel function indicative of incommensurate magnetic structure or LRO. The resulting μSR frequency is displayed in Fig. 11. The relaxation of the 1/3 tail could be successfully described by taking the root of an exponential function, $\exp(\sqrt{\lambda_L t})$, typical for inhomogeneous magnetic dynamics. The dynamic relaxation rate λ_L is shown as a function of temperature in Fig. 12. It reveals the characteristic divergence at the phase transition and remains nonzero

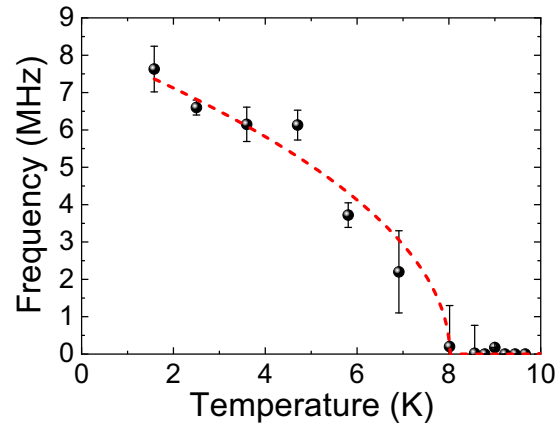

FIG. 11. μSR frequency measuring the magnetic order parameter as a function of temperature. The red dashed line represents a mean-field power law [according to Eq. (2) with $2\beta = 0.5$] with a critical temperature $T_c = 8.1(3)$ K and zero frequency $\nu_0 = 8.2(2)$ MHz.

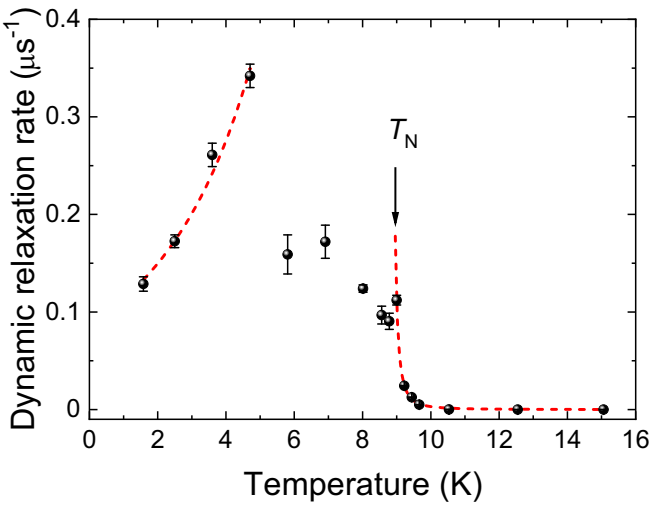

FIG. 12. Dynamic relaxation rate as a function of temperature showing a first peak at the Néel temperature and a second peak below T_N at 5 K. The dashed lines are guides to the eye.

at low temperatures as already discussed qualitatively above, indicating a persistent spin dynamics in the low megahertz region. The second peak in the dynamic relaxation rate at ∼5 K may arise since in this temperature range the μSR spectra are collected in the mixed ordered and paramagnetic state. The dynamical relaxation rate hence reflects a superposition of a critical slowing down of the paramagnetic volume fraction and a decrease due to spin wave excitations in the ordered state.

IV. DISCUSSION AND CONCLUSION

Law *et al.* [31] have analyzed the bulk magnetic and thermal properties and also performed density functional theory (DFT) calculations of the spin-exchange parameters of $CuCrO_4$. They found long-range magnetic order below about 8.2 K and type-II multiferroic behavior [31]. The spin-exchange parameters derived from their DFT calculations indicated one-dimensional behavior with not only dominant NN AFM exchange but also sizable (∼50%) NNN AFM exchange interaction. A strong external magnetic field suppresses multiferroicity, but full magnetization saturation is not reached in fields up to ∼60 T. An indication of a plateau in the magnetization is also not seen. A rough estimate of the saturation field for a spin $S = 1/2$ Heisenberg chain according to [42]

$$\mu_0 H_{\rm sat} = \frac{4J_{\rm NN}}{g\mu_{\rm B}},$$

using $J_{\rm NN} \approx 55$ K as derived from the DFT calculations and fits of the low field magnetic susceptibility [31], indicates a saturation field of about 80 T consistent with the experimental findings.

The results reported here using neutron powder diffraction and muon-spin rotation consistently prove that the Cu^{2+} magnetic moments in $CuCrO_4$ order with an incommensurate magnetic structure, similar to many other 3*d* transition metal phosphates, vanadates, or anhydrous sulfates that crystallize with the $CrVO_4$ crystal structure type [22–25,27]. Our neutron powder diffraction investigation shows that the Cu moments arrange with a helicoidal spin spiral with an easy $a - c$ plane propagation along the crystallographic *c* axis, i.e., along ribbon chains, and FM order along the crystallographic *a* and *b* directions (see Fig. 7). The Cu atoms reside in trans-edge connected Jahn-Teller elongated oxygen octahedra with their equatorial planes slightly corrugated enclosing an angle of ∼167° with the neighboring equatorial planes. The magnetic moment, refined from the difference pattern 1.9 K minus 9 K, amounts to 0.48 $\mu_{\rm B}$, significantly reduced from the 1 $\mu_{\rm B}$ expected from the spin $S = 1/2$ state with a *g* factor close to 2 as implied by the $3d^9$ configuration of the Cu^{2+} cations with half-filled $d_{x^2-y^2}$ orbitals.

The observation of incommensurate magnetic order is consistent with the multiferroic behavior of $CuCrO_4$ found by Law *et al.* [31]. Allowing for a corrugation of the moments out of the $a - c$ planes and implying a canting angle of ∼12° out of the equatorial plane along [010], the moment component along the crystallographic *b* axis refines to about 0.04 $\mu_{\rm B}$, too small to significantly improve the refinement.

The source of incommensurate spiral order and multiferroic behavior of $CuCrO_4$ is the competition of $J_{\rm NN}$ and $J_{\rm NNN}$ spin-exchange interactions, analogous to what has been observed, e.g., for $LiCuVO_4$ and the cupric halides, CuX_2 (X = Cl, Br) [8–12,30,31,43,44]. However, unlike the latter systems, where $J_{\rm NN}$ turned out to be FM, $CuCrO_4$ offers the alternative scenario with both intrachain spin-exchange parameters being AFM, similar to the inorganic spin-Peierls compound $CuGeO_3$, for example [45,46].

The pitch angle between neighboring Cu moments refined from the difference pattern amounts to ∼100°. Comparing this result with the simple energy relation for NN-NNN frustrated chains with classical spin moments *S*,

$$E(q_c)/(J_{\rm NN}S^2) = \cos(q_c) + (J_{\rm NNN}/J_{\rm NN})\cos(2q_c), \qquad (4)$$

for $J_{\rm NN} \approx 2 \times J_{\rm NNN}$, the energy minimum is attained at a pitch angle of ∼120°, somewhat away from our experimental result.

The position of the energy minimum and the pitch angle do not change if we assume the FM spin exchange, J_a, between moments along the *a* axis, i.e., between neighboring chains. Alternatively, with spin exchange along the *a* axis as reported by Law *et al.* [31] ($|J_a|/|J_{\rm NN}| \sim 0.2$), the Cu moments in $CuCrO_4$ may be considered as spin ladders with spin frustration along the legs and weak FM coupling along the rungs. Further distant interchain spin exchange and/or quantum effects may account for the deviation of the pitch angle calculated from Eq. (4) from the experimental findings. The phase diagram for NN-NNN frustrated spin $S = 1/2$ quantum spin chains was intensively investigated by Furukawa *et al.* [5] and Sato *et al.* [6] about a decade ago. The ground-state phase diagram of frustrated NN-NNN spin $S = 1/2$ chains for FM NN and AFM NNN spin exchange ($J_{\rm NN}/J_{\rm NNN} < 0$) for small easy-plane exchange anisotropy contains an extended sector supporting a chiral phase. In the phase space for $J_{\rm NN}/J_{\rm NNN} > 0$, rather, spin-singlet dimer order or a collinear AFM LRO are predicted, in disagreement with our experimental findings [5,6,47]. At present, one can only speculate whether this difference is due to asymmetry of the spin exchange or interchain exchange.

Concerning the general spin-exchange scenario, $CuCrO_4$ resembles the spin-Peierls compound $CuGeO_3$, where NN spin exchange and NNN spin exchange were also both found to be AFM. However, in $CuGeO_3$ the ratio J_{NNN}/J_{NN} was determined to range between 0.24 and 0.36, somewhat lower than in $CuCrO_4$ [45,46,48]. As is seen from the μSR dynamical relaxation rate (cf. Fig. 12) the LRO phase of $CuCrO_4$ still exhibits some dynamics, possibly related to fluctuations of the spin helices, with fluctuation rates in the megahertz region but slowing down towards lower temperatures. The measurements of the dielectric permittivity in pulsed magnetic fields evidence a gradual transition from the multiferroic phase to a nonmultiferroic phase above ~25 T. We tentatively assign this transition to a field-induced transformation of the helicoidal magnetic structure into a commensurate, possibly collinear magnetic structure.

ACKNOWLEDGMENTS

We acknowledge the support of the HLD at HZDR, a member of the European Magnetic Field Laboratory (EMFL); the Deutsche Forschungsgemeinschaft (DFG) through SFB 1143; and the Würzburg-Dresden Cluster of Excellence on Complexity and Topology in Quantum Matter ct.qmat (EXC 2147, Project No. 390858490). Part of this work was performed at the Swiss Muon Source, Paul Scherrer Institute, Villigen, Switzerland. We are indebted to V. Pomjakushin for expert help with the HRPT experiments.

[1] D. Khomskii, Classifying multiferroics: Mechanisms and effects, Physics **2**, 20 (2009).

[2] O. Auciello, J. F. Scott, and R. Ramesh, The physics of ferroelectric memories, Phys. Today **51**(7), 22 (1998).

[3] N. A. Spaldin, S.-W. Cheong, and R. Ramesh, Multiferroics: Past, present, and future, Phys. Today **63**(10), 38 (2010).

[4] A. M. Läuchli, J. Sudan, and A. Lüscher, The frustrated ferromagnetic $S = 1/2$ Heisenberg chain in a magnetic field – How multipolar spin correlations emerge from magnetically ordered states, J. Phys.: Conf. Ser. **145**, 012057 (2009).

[5] S. Furukawa, M. Sato, and S. Onoda, Chiral Order and Electromagnetic Dynamics in One-Dimensional Multiferroic Cuprates, Phys. Rev. Lett. **105**, 257205 (2010).

[6] M. Sato, S. Furukawa, S. Onoda, and A. Furusaki, Competing phases in spin-1/2 J_1-J_2 chain with easy-plane anisotropy, Mod. Phys. Lett. B **25**, 901 (2011).

[7] S.-L. Drechsler, J. Richter, R. Kuzian, J. Málek, N. Tristan, B. Büchner, A. Moskvin, A. Gippius, A. Vasiliev, O. Volkova, A. Prokofiev, H. Rakoto, J.-M. Broto, W. Schnelle, M. Schmitt, A. Ormeci, C. Loison, and H. Rosner, Helimagnetism and weak ferromagnetism in edge-shared chain cuprates, J. Magn. Magn. Mater. **316**, 306 (2007).

[8] B. J. Gibson, R. K. Kremer, A. V. Prokofiev, W. Assmus, and G. J. McIntyre, Incommensurate antiferromagnetic order in the S = 1/2 quantum chain compound $LiCuVO_4$, Phys. B (Amsterdam) **350**, E253 (2004).

[9] M. G. Banks, R. K. Kremer, C. Hoch, A. Simon, B. Ouladdiaf, J.-M. Broto, H. Rakoto, C. Lee, and M.-H. Whangbo, Magnetic ordering in the frustrated Heisenberg chain system cupric chloride $CuCl_2$, Phys. Rev. B **80**, 024404 (2009).

[10] J. M. Law, C. Hoch, M.-H. Whangbo, and R. K. Kremer, Description of anhydrous (black) dioptase as a $S = 1/2$ uniform antiferromagnetic chain system, Z. Anorg. Allg. Chem. **636**, 54 (2010).

[11] L. Zhao, T.-L. Hung, C.-C. Li, Y.-Y. Chen, M.-K. Wu, R. K. Kremer, M. G. Banks, A. Simon, M.-H. Whangbo, C. Lee, J. S. Kim, I. Kim, and K. H. Kim, $CuBr_2$ a new multiferroic material with high critical temperature, Adv. Mater. **24**, 2469 (2012).

[12] C. Lee, J. Liu, M.-H. Whangbo, H.-J. Koo, R. K. Kremer, and A. Simon, Investigation of the spin exchange interactions and the magnetic structure of the high-temperature multiferroic $CuBr_2$, Phys. Rev. B **86**, 060407(R) (2012).

[13] M. Mourigal, M. Enderle, B. Fåk, R. K. Kremer, J. M. Law, A. Schneidewind, A. Hiess, and A. Prokofiev, Evidence of a Bond-Nematic Phase in $LiCuVO_4$, Phys. Rev. Lett. **109**, 027203 (2012).

[14] A. Orlova, E. L. Green, J. M. Law, D. I. Gorbunov, G. Chanda, S. Krämer, M. Horvatić, R. K. Kremer, J. Wosnitza, and G. L. J. A. Rikken, Nuclear Magnetic Resonance Signature of the Spin-Nematic Phase in $LiCuVO_4$ at High Magnetic Fields, Phys. Rev. Lett. **118**, 247201 (2017).

[15] H. Xiang, C. Lee, H.-J. Koo, X. Gong, and M.-H. Whangbo, Magnetic properties and energy-mapping analysis, Dalton Trans. **42**, 823 (2013).

[16] M.-H. Whangbo, H.-J. Koo, and R. K. Kremer, Spin exchanges between transition metal ions governed by the ligand p-orbitals in their magnetic orbitals, Molecules **26**, 531 (2021).

[17] K. Caslin, R. K. Kremer, F. S. Razavi, A. Schulz, A. Muñoz, F. Pertlik, J. Liu, M.-H. Whangbo, and J. M. Law, Characterization of the spin-$\frac{1}{2}$ linear-chain ferromagnet $CuAs_2O_4$, Phys. Rev. B **89**, 014412 (2014).

[18] K. Caslin, R. K. Kremer, F. S. Razavi, M. Hanfland, K. Syassen, E. E. Gordon, and M.-H. Whangbo, Competing Jahn-Teller distortions and hydrostatic pressure effects in the quasi-one-dimensional quantum ferromagnet $CuAs_2O_4$, Phys. Rev. B **93**, 022301 (2016).

[19] N. Seferiadis and H. R. Oswald, Refinement of the structure of copper(II) chromate from single-crystal data, Acta Cryst. C **43**, 10 (1987).

[20] E. J. Baran, Materials belonging to the $CrVO_4$, structure type: preparation, crystal chemistry and physicochemical properties, J. Mater. Sci. **33**, 2479 (1998).

[21] B. C. Frazer and P. J. Brown, Antiferromagnetic Structure of $CrVO_4$ and the Anhydrous Sulfates of Divalent Fe, Ni, and Co, Phys. Rev. **125**, 1283 (1962).

[22] G. Will, B. C. Frazer, G. Shirane, D. E. Cox, and P. J. Brown, Cycloidal spin configuration of orthorhombic $MnSO_4$, J. Appl. Phys. **36**, 1095 (1965).

[23] G. Will, B. C. Frazer, G. Shirane, D. E. Cox, and P. J. Brown, Magnetic Structure of $MnSO_4$, Phys. Rev. **140**, A2139 (1965).

[24] J. P. Attfield, P. D. Battle, and A. K. Cheetham, The spiral magnetic structure of β-chromium(III) orthophosphate ($\beta - CrPO_4$), J. Solid State Chem. **57**, 357 (1985).

[25] J. P. Wright, J. P. Attfield, W. I. F. David, and J. B. Forsyth, High-resolution powder neutron diffraction study of helimagnetic order in $CrP_{1-x}V_xO_4$ solid solutions, Phys. Rev. B **62**, 992 (2000).

[26] N. Kinomura, F. Muto, and M. Koizumi, Preparation of transition metal orthophosphates, MPO_4, and their magnetic properties, J. Solid State Chem. **45**, 252 (1982).

[27] R. Glaum, M. Reehuis, N. Stüßer, U. Kaiser, and F. Reinauer, Neutron diffraction study of the nuclear and magnetic structure of the $CrVO_4$ type phosphates $TiPO_4$ and VPO_4, J. Solid State Chem. **126**, 15 (1996).

[28] T. Yamauchi and Y. Ueda, Isostructural transition metal orthophosphates with linear chain of $S = 1/2$, 1 and 3/2, J. Magn. Magn. Mater. **177–181**, 705 (1998).

[29] S. Luo and K. Wang, Multiferroicity in cycloidal spiral spin magnet β - $CrPO_4$, J. Alloys Compd. **726**, 833 (2017).

[30] J. M. Law, C. Hoch, R. Glaum, I. Heinmaa, R. Stern, J. Kang, C. Lee, M.-H. Whangbo, and R. K. Kremer, Spin-Peierls transition in the $S = \frac{1}{2}$ compound $TiPO_4$ featuring large intrachain coupling, Phys. Rev. B **83**, 180414(R) (2011).

[31] J. M. Law, P. Reuvekamp, R. Glaum, C. Lee, J. Kang, M.-H. Whangbo, and R. K. Kremer, Quasi-one-dimensional antiferromagnetism and multiferroicity in $CuCrO_4$, Phys. Rev. B **84**, 014426 (2011).

[32] M. Bykov, J. Zhang, A. Schönleber, A. Wölfel, S. I. Ali, S. van Smaalen, R. Glaum, H.-J. Koo, M.-H. Whangbo, P. G. Reuvekamp, J. M. Law, C. Hoch, and R. K. Kremer, Spin-Peierls distortions in $TiPO_4$, Phys. Rev. B **88**, 184420 (2013).

[33] D. Wulferding, A. Möller, K.-Y. Choi, Y. G. Pashkevich, R. Y. Babkin, K. V. Lamonova, P. Lemmens, J. M. Law, R. K. Kremer, and R. Glaum, Lattice and orbital fluctuations in $TiPO_4$, Phys. Rev. B **88**, 205136 (2013).

[34] M. Bykov, E. Bykova, M. Hanfland, H.-P. Liermann, R. K. Kremer, R. Glaum, L. Dubrovinsky, and S. van Smaalen, High-pressure phase transformations in $TiPO_4$: A route to pentacoordinated phosphorus, Angew. Chem. Int. Ed. **55**, 15053 (2016).

[35] C. K. Majumdar and D. K. Ghosh, On next-nearest-neighbor interaction in linear chain. I, J. Math. Phys. **10**, 1388 (1969).

[36] C. K. Majumdar and D. K. Ghosh, On next-nearest-neighbor interaction in linear chain. II, J. Math. Phys. **10**, 1399 (1969).

[37] P. Fischer, G. Frey, M. Koch, M. Könnecke, V. Pomjakushin, J. Schefer, R. Thut, N. Schlumpf, R. Bürge, U. Greuter, S. Bondt, and E. Berruyer, High-resolution powder diffractometer HRPT for thermal neutrons at SINQ, Phys. B (Amsterdam) **276–278**, 146 (2000).

[38] T. C. Hansen, P. F. Henry, H. E. Fischer, J. Torregrossa, and P. Convert, The D20 instrument at the ILL: a versatile high-intensity two-axis neutron diffractometer, Meas. Sci. Technol. **19**, 034001 (2008).

[39] J. Rodríguez-Carvajal, Recent advances in magnetic structure determination by neutron powder diffraction, Phys. B (Amsterdam) **192**, 55 (1993).

[40] Y. Skourski, M. D. Kuz'min, K. P. Skokov, A. V. Andreev, and J. Wosnitza, High-field magnetization of Ho_2Fe_{17}, Phys. Rev. B **83**, 214420 (2011).

[41] M. Doerr, W. Lorenz, T. Neupert, M. Loewenhaupt, N. V. Kozlova, J. Freudenberger, M. Bartkowiak, E. Kampert, and M. Rotter, Simultaneous measurement of magnetization and magnetostriction in 50T pulsed high magnetic fields, Rev. Sci. Instrum. **79**, 063902 (2008).

[42] I. Affleck and M. Oshikawa, Field-induced gap in Cu benzoate and other $S = \frac{1}{2}$ antiferromagnetic chains, Phys. Rev. B **60**, 1038 (1999).

[43] F. Schrettle, S. Krohns, P. Lunkenheimer, J. Hemberger, N. Büttgen, H.-A. Krug von Nidda, A. V. Prokofiev, and A. Loidl, Switching the ferroelectric polarization in the $S = 1/2$ chain cuprate $LiCuVO_4$ by external magnetic fields, Phys. Rev. B **77**, 144101 (2008).

[44] A. Ruff, P. Lunkenheimer, H.-A. Krug von Nidda, S. Widmann, A. Prokofiev, L. Svistov, A. Loidl, and S. Krohns, Chirality-driven ferroelectricity in $LiCuVO_4$, npj Quantum Mater. **4**, 24 (2019).

[45] J. Riera and A. Dobry, Magnetic susceptibility in the spin-Peierls system $CuGeO_3$, Phys. Rev. B **51**, 16098 (1995).

[46] G. Castilla, S. Chakravarty, and V. J. Emery, Quantum Magnetism of $CuGeO_3$, Phys. Rev. Lett. **75**, 1823 (1995).

[47] K. Okunishi and T. Tonegawa, Magnetic phase diagram of the $S = 1/2$ antiferromagnetic zigzag spin chain in the strongly frustrated region: Cusp and plateau, J. Phys. Soc. Jpn. **72**, 479 (2003).

[48] K. Fabricius, A. Klümper, U. Löw, B. Büchner, T. Lorenz, G. Dhalenne, and A. Revcolevschi, Reexamination of the microscopic couplings of the quasi-one-dimensional antiferromagnet $CuGeO_3$, Phys. Rev. B **57**, 1102 (1998).